

# Polaron optical absorption in congruent lithium niobate from time-dependent density-functional theory

Michael Friedrich,\* W. G. Schmidt, and Arno Schindlmayr  
*Department Physik, Universität Paderborn, 33095 Paderborn, Germany*

Simone Sanna

*Institut für Theoretische Physik, Justus-Liebig-Universität Gießen, Heinrich-Buff-Ring 16, 35392 Gießen, Germany*

(Received 24 July 2017; published 11 October 2017)

The optical properties of congruent lithium niobate are analyzed from first principles. The dielectric function of the material is calculated within time-dependent density-functional theory. The effects of isolated intrinsic defects and defect pairs, including the  $\text{Nb}_{\text{Li}}^{4+}$  antisite and the  $\text{Nb}_{\text{Li}}^{4+}$ - $\text{Nb}_{\text{Nb}}^{4+}$  pair, commonly addressed as a bound polaron and bipolaron, respectively, are discussed in detail. In addition, we present further possible realizations of polaronic and bipolaronic systems. The absorption feature around 1.64 eV, ascribed to small bound polarons [O. F. Schirmer *et al.*, *J. Phys. Condens. Matter* **21**, 123201 (2009)], is nicely reproduced within these models. Among the investigated defects, we find that the presence of bipolarons at bound interstitial-vacancy pairs  $\text{Nb}_{\text{V}}\text{-V}_{\text{Li}}$  can best explain the experimentally observed broad absorption band at 2.5 eV. Our results provide a microscopic model for the observed optical spectra and suggest that, besides  $\text{Nb}_{\text{Li}}$  antisites and Nb and Li vacancies, Nb interstitials are also formed in congruent lithium-niobate samples.

DOI: [10.1103/PhysRevMaterials.1.054406](https://doi.org/10.1103/PhysRevMaterials.1.054406)

## I. INTRODUCTION

Lithium niobate ( $\text{LiNbO}_3$ , LN) is a material that combines a variety of remarkable physical properties, such as large acousto-optical, piezoelectric, electro-optical, and nonlinear optical coefficients. The LN employed in technical applications is usually grown from a congruent melt using the Czochralski technique. The crystals grown in this way show a Li:Nb ratio of 48.5:51.5; that is, they are strongly lithium deficient. Congruent lithium niobate (CLN) is thus characterized by a high concentration of intrinsic defects, especially  $\text{Nb}_{\text{Li}}^{5+}$  antisites [1]. Besides the defects directly due to the lithium deficiency, additional defects must form in order to maintain charge neutrality, as each  $\text{Nb}_{\text{Li}}^{5+}$  antisite carries four excess positive charges relative to the  $\text{Li}_{\text{Li}}^+$  ion it replaces. Different charge-compensation mechanisms have been discussed in this context. On the basis of density measurements, Lerner *et al.* [2] proposed in 1968 that four lithium vacancies ( $\text{V}_{\text{Li}}$ ) compensate one  $\text{Nb}_{\text{Li}}^{5+}$  antisite (Li-vacancy model). Subsequently, another defect model supported by nuclear magnetic resonance spectroscopy was suggested by Peterson and Carnevale [3]. In this Nb-vacancy model, five  $\text{Nb}_{\text{Li}}^{5+}$  antisites are compensated by four niobium vacancies ( $\text{V}_{\text{Nb}}$ ). Structure analysis by x-ray or neutron powder diffraction equivocally favored either the Li-vacancy model [4–6] or the Nb-vacancy model [7].

A scenario reconciling the two charge-compensation mechanisms was proposed by Donnerberg *et al.* [8], who investigated regions of ilmenite-like stacking in lithium niobate, an idea already suggested by Smyth [9] based on semiempirical calculations. The ilmenite structure is equivalent to the lithium niobate structure but exhibits a different cationic stacking sequence, shown in Fig. 1(e). Calorimetric measurements [10] show that this structure is only 0.1 eV per formula unit higher

in energy than stoichiometric LN, suggesting that regions of ilmenite stacking may indeed occur locally in congruent lithium niobate. An alternative model featuring a mixture of niobium antisites and interstitial niobium atoms in the empty octahedra ( $\text{Nb}_{\text{V}}^{5+}$ ), charge compensated by lithium vacancies, was proposed by Zotov *et al.* [6], who reported that it described their x-ray and neutron-powder-diffraction measurements at the same level of significance of the goodness-of-fit factors as the Li-vacancy model.

Nowadays, the Li-vacancy model is widely accepted as the principal structural element of CLN. It is also supported by density-functional-theory calculations using the generalized gradient approximation [11] as well as hybrid functionals [12], which are designed to further improve the description of the exchange-correlation energy. The formation of niobium vacancies cannot be excluded [13] and may constitute an additional charge-compensation source, however. In any case, the lattice structure of CLN is expected to differ substantially from that of ideal stoichiometric LN displayed in Fig. 1(a) and to contain a large variety of defect centers influencing its optical properties. The latter are usually interpreted within the polaron concept [14].

Electronic small polarons are formed when an electron becomes trapped at essentially one lattice site due to the short-range interaction of the charge carrier with the surrounding lattice. Polarons tend to localize at crystal defects, especially at positively charged impurities, due to the attractive Coulomb potential and the additional lattice distortion. Metastable bound polarons with a thermally induced or photoexcited peak at around 1.64 eV, as well as bound bipolarons characterized by a broad peak in the absorption spectrum at around 2.5 eV, dominate the optical properties of lithium niobate [14–16]. This assignment is supported by rich evidence, whereas alternative explanations for the two absorption peaks are unlikely, as discussed in [14].  $\text{Nb}_{\text{Li}}$  antisites and  $\text{Nb}_{\text{Li}}\text{-Nb}_{\text{Nb}}$  pairs are commonly assumed to be responsible for the formation of small bound polarons and bipolarons, respectively, but

\*michael.friedrich@uni-paderborn.de

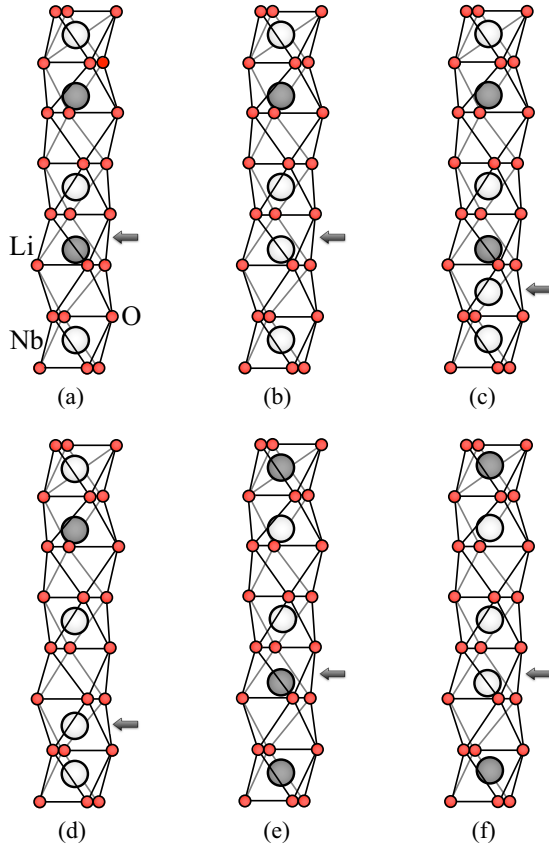


FIG. 1. (a) Defect-free stoichiometric lithium niobate is characterized by the Nb-vacancy-Li stacking (from bottom to top) of the cations inside the oxygen octahedra. Intrinsic defects include (b) isolated  $\text{Nb}_{\text{Li}}$  antisites and (c)  $\text{Nb}_{\text{V}}$  interstitials at structural vacancies inside empty oxygen octahedra as well as (d) interstitial niobium atoms paired with Li vacancies ( $\text{Nb}_{\text{V}}\text{-V}_{\text{Li}}$ ). (e) The ilmenite structure is equivalent to the lithium-niobate structure but has a slightly different cationic stacking sequence. (f) In this structure, we also consider  $\text{Nb}_{\text{Li}}$  antisites. The atoms referenced as  $X$  in Tables I, II, and III are marked with arrows.

there is no direct experimental evidence for a conclusive assignment of the spectral features to a particular defect model. The experimental difficulties arise in part from the fact that bipolarons are diamagnetic and hence silent in electron paramagnetic resonance. In addition, a thorough theoretical investigation of intrinsic defects in CLN and their optical properties beyond the independent-particle approximation (IPA) is still missing.

Electronic-structure calculations of bound polarons modeled by  $\text{Nb}_{\text{Li}}$  antisites in the ideal LN lattice were carried out by Nahm and Park [17] and support the polaron scenario described by Schirmer *et al.* [14]. Optical-response calculations within the IPA also indicate polaron absorption inside the electronic band gap [12], but such independent-particle calculations neglect the strong many-body effects in lithium niobate [18] and at localized defect states in general [19]. While many-body perturbation theory allows, in principle, for the accurate calculation of quasiparticle energies and excitonic effects, it is prohibitively expensive for the large supercells required to model the defect structures realistically. Fortunately, time-

dependent density-functional theory (TDDFT) provides an alternative and computationally less expensive route to obtain the optical response [20]. However, the exchange-correlation kernel for extended systems must then include a long-range contribution (LRC) inversely proportional to the square of the wave vector [21], which describes excitonic effects in qualitative agreement with the Bethe-Salpeter equation [22].

In this work, we present a thorough theoretical study of intrinsic defects in lithium niobate with particular attention to their influence on the optical properties of the material. To this effect, we perform spin-polarized calculations that go beyond the IPA by including many-body effects within a TDDFT-LRC approach. In particular, we investigate several possible realizations of (bi)polarons, including electrons localized at  $\text{Nb}_{\text{Li}}$  antisites in stoichiometric LN (SLN), at  $\text{Nb}_{\text{V}}$  interstitials, and at  $\text{Nb}_{\text{Li}}$  antisites in the ilmenite structure (ILN). Our results confirm the polaron scenario proposed by Schirmer *et al.* [14] and provide a microscopic theoretical model for polaronic defects in lithium niobate.

## II. COMPUTATIONAL METHOD

For the ground-state total-energy calculations we use (spin-polarized) density-functional theory (DFT) as implemented in the QUANTUM ESPRESSO package [23]. Optimized norm-conserving Vanderbilt pseudopotentials [24] are chosen to model the electron-ion interaction. The Li  $1s$  and  $2s$  orbitals, the O  $2s$  and  $2p$  orbitals, and the Nb  $4s$ ,  $4p$ ,  $4d$ , and  $5s$  orbitals are treated explicitly as valence states. The cutoff energy for the plane-wave basis set is 1150 eV, sufficient to converge the total energy per unit cell within 5 meV. The Brillouin zone is sampled with a shifted  $4 \times 4 \times 4$  Monkhorst-Pack mesh for the primitive unit cell, which contains ten atoms. For the simulation of defects, we use supercells comprising either  $2 \times 2 \times 2$  or  $3 \times 3 \times 3$  primitive unit cells, equivalent to 80 or 270 atoms before the insertion of defects. From the perspective of materials science, the different supercell sizes allow us to simulate different defect concentrations: One  $\text{Nb}_{\text{Li}}$  antisite in a  $2 \times 2 \times 2$  supercell corresponds to a Li:Nb ratio of 88%, while the same defect in the larger  $3 \times 3 \times 3$  supercell corresponds to 96%. In accordance with the reduced volume of the Brillouin zone, the sampling is performed with  $3 \times 3 \times 3$  and  $2 \times 2 \times 2$  mesh points in these cases, respectively. The convergence threshold for the Hellmann-Feynman forces is set to 0.01 eV/Å. We use the modified Perdew-Burke-Ernzerhof parametrization for solids (PBEsol) [25] for the exchange-correlation energy, a generalized gradient approximation that accurately reproduces the experimental lattice constants of solids, including LN and related materials [26–28].

For defects involving Nb atoms, it is important to treat the strong localization of electrons in the  $d$  orbitals properly, as pointed out by Nahm and Park [17] and by Sanson *et al.* [29]. For this reason, we use the DFT+ $U$  approach of Cococcioni and de Gironcoli [30] to improve the description of strong electronic correlation. This approach largely solves the interaction issues affecting DFT and has a major effect on localized defect levels, such as the polaron energies inside the band gap studied in this work. It incorporates an effective parameter  $U_{\text{eff}} = U - J$ , defined as the difference between the on-site Coulomb interaction  $U$  and the on-site exchange

interaction  $J$ . Here we set  $U_{\text{eff}} = 4 \text{ eV}$ , the same value as in [17,29], so that our results can be compared with the existing literature.

As DFT and DFT+ $U$  based on the generalized gradient approximation underestimate the electronic band gap, we also perform calculations with the Heyd-Scuseria-Ernzerhof hybrid functional (HSE06) [31], which is based on a PBE-type exchange-correlation functional but replaces 25% of the short-range component of the exchange energy with nonlocal Hartree-Fock exchange. In this way, we can assess the influence of different computational approaches on the description of defects. Due to the much larger computational effort, we limit these hybrid-functional calculations to the  $2 \times 2 \times 2$  supercell. The cutoff energy is kept at 1150 eV, which ensures convergence of the total energy per unit cell within 5 meV. The lattice constants are fixed at their PBEsol values, but we again relax the internal atomic positions with a force threshold of 0.01 eV/Å.

Following the structure optimization, we determine the optical properties using TDDFT within the linear response. The calculations are carried out with the YAMBO code [32]. When constructing the independent-particle response function, we use the Kohn-Sham eigenvalues from PBEsol but apply a scissors shift to the conduction bands that adjusts the electronic energy gap to the larger HSE06 value; a full TDDFT implementation based on hybrid functionals is currently not feasible for the systems considered here, as the computational effort would be prohibitive. For the exchange-correlation kernel we use the static long-range contribution

$$f_{\mathbf{G}}^{\text{xc,LRC}}(\mathbf{q}) = -\frac{\alpha}{|\mathbf{q} + \mathbf{G}|^2}, \quad (1)$$

where  $\mathbf{G}$  is a reciprocal lattice vector and the wave vector  $\mathbf{q}$  of the incident light tends to zero in the optical limit. The parameter  $\alpha$  is set to 0.44. Further computational details as well as performance tests of the LRC can be found in [33], where we used the same approach to investigate the effect of extrinsic doping by titanium indiffusion on the optical properties of LN. In that study, we also tested various flavors of the so-called bootstrap approach [34,35], which expresses the exchange-correlation kernel in terms of the inverse dielectric function, but we found the differences between the LRC and the bootstrap approach to be minor for lithium niobate [33]. Therefore, the LRC is used exclusively in this work.

In calculations for the primitive unit cell of SLN, we include 1500 reciprocal lattice vectors in the Coulomb potential and the exchange-correlation kernel and 350 electronic energy bands. The Brillouin-zone sampling is increased with respect to the ground-state DFT calculations and employs  $6 \times 6 \times 6$   $\Gamma$ -centered mesh points. With these parameters, the imaginary part of the dielectric function is converged within a tolerance of  $10^{-4}$ .

When calculating the optical properties of systems containing defects, we use 2700 reciprocal lattice vectors, 640 electronic energy bands, and a  $3 \times 3 \times 3$   $\mathbf{k}$ -point sampling of the Brillouin zone for the smaller  $2 \times 2 \times 2$  supercell. For the larger  $3 \times 3 \times 3$  supercell, we use 4000 lattice vectors, 1620 bands, and  $2 \times 2 \times 2$   $\mathbf{k}$  points. These convergence parameters are sufficient to determine the dielectric function within numerical error bars of 2%.

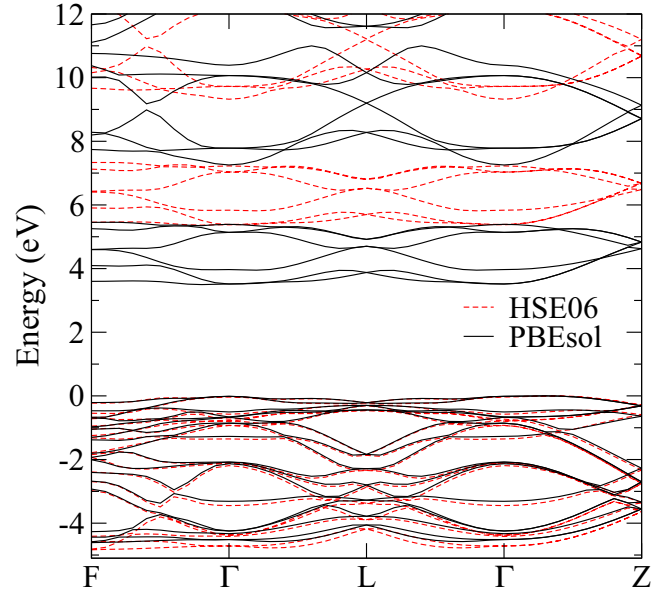


FIG. 2. Calculated electronic band structure of stoichiometric lithium niobate. The HSE06 hybrid exchange-correlation functional widens the fundamental band gap with respect to PBEsol but yields an almost identical dispersion.

### III. RESULTS

#### A. Stoichiometric lithium niobate

The calculated lattice constants of the primitive rhombohedral unit cell,  $a_{\text{H}} = 5.133 \text{ \AA}$  and  $c_{\text{H}} = 13.828 \text{ \AA}$ , are only marginally (0.35%) smaller than the experimental values [36]. This difference arises in part from the neglect of thermal expansion in our simulations. The electronic band structures obtained with the PBEsol and HSE06 exchange-correlation functionals are displayed in Fig. 2. As intended, the hybrid functional widens the fundamental band gap compared to the PBEsol value of 3.5 eV, but the dispersion of the energy levels remains essentially unchanged. Furthermore, the HSE06 band structure accurately reproduces the results of Riefer *et al.* [37], which stem from a self-consistent solution of the  $GW_0$  quasiparticle equation and additionally take electron-phonon coupling into account. In fact, the HSE06 band gap of 5.4 eV obtained here exactly matches the value derived in [37]. This provides a further justification for the present approach, which approximates many-body effects in the optical absorption by combining TDDFT-LRC with a scissors operator derived from hybrid DFT. Experimental values of the fundamental band gap ranging from 3.3 to 4.3 eV [38–41] were extrapolated from optical measurements. However, these values cannot be directly compared with the electronic band gap, as the electron-hole interaction leads to a substantial difference between optical and electronic gaps in LN [42]. Also, the influence of the intrinsic defects present in congruent LN will further reduce the gap by about 0.5 eV (see Fig. 3).

Significantly larger lattice constants of  $a_{\text{H}} = 5.198 \text{ \AA}$  and  $c_{\text{H}} = 14.197 \text{ \AA}$  are obtained for the ilmenite variant of LN due to the different atomic structure. Compared to SLN, this is an increase of 1.3% for  $a_{\text{H}}$  and 2.7% for  $c_{\text{H}}$ . The HSE06 functional widens the band gap from 4.0 to 5.8 eV. According

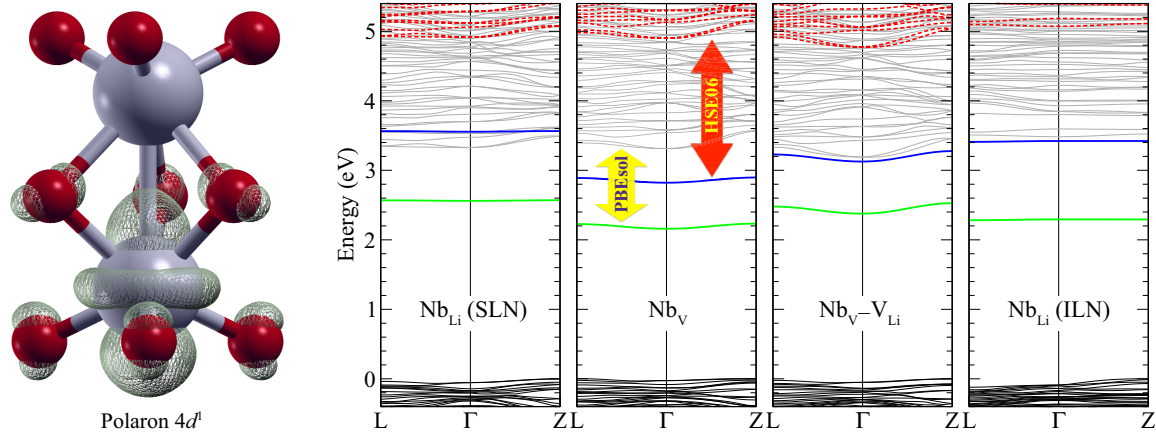


FIG. 3. Electronic structure resulting from the presence of a polaron in the material. Left: The electronic charge density associated with the  $\text{Nb}_{\text{Li}}^{4+}$  ( $4d^1$ ) polaron level in SLN is localized at the Nb atom. This is true for all defect types. Right: Electronic band structures for all considered defects. Only the spin-up channel is shown, as the spin-down channel has no defect state inside the band gap. The black, gray, and green curves refer to DFT+ $U$  calculations with the PBEsol functional. The HSE06 hybrid functional raises the conduction bands (red dashed lines) and shifts the position of the polaron level (blue). To facilitate reading, the arrows indicating the energy separation between the occupied polaron level and the unoccupied conduction bands are not added to all panels.

to our results, the energy difference between lithium niobate in its ground-state structure and in the ilmenite structure amounts to 0.24 eV (PBEsol) and 0.21 eV (HSE06) per unit cell. These numbers agree well with the experimental findings of Mehta *et al.* [10], who estimated the enthalpy difference to be  $0.20 \pm 0.08$  eV. Earlier calculations on the basis of an ionic shell model had predicted 0.1 eV per unit cell [8].

### B. Congruent lithium niobate

If a  $\text{Li}_{\text{Li}}^+$  ion is substituted by a  $\text{Nb}_{\text{Li}}^{5+}$  ion, four nominal additional positive charges are introduced into the supercell. In real samples, these excess charges are most likely compensated by lithium vacancies and, to a minor extent, by niobium vacancies situated elsewhere in the material. In this work, we study several distinct defect types as possible centers for the formation of polarons and bipolarons. For this purpose, we place an isolated charged point defect into a supercell, and we compensate the excess ionic charges by adding a spatially homogeneous negative background charge with the same integral value but opposite sign as the excess ionic charges of the defect, so that the entire supercell is charge neutral. We model not only  $\text{Nb}_{\text{Li}}$  antisites in this way but also  $\text{Nb}_{\text{V}}$  interstitials,  $\text{Nb}_{\text{V}}\text{-V}_{\text{Li}}$  complexes, and  $\text{Nb}_{\text{Li}}$  antisites in the ilmenite stacking. Like the Li  $2s$  orbitals of the original  $\text{Li}^+$  ion, the Nb  $4d$  orbitals of the  $\text{Nb}^{5+}$  defect atom are initially empty because the valence electrons in the outermost shell are transferred to the oxygen atoms in both cases. Consequently, we denote this electronic configuration as  $\text{Nb}^{5+}$  ( $4d^0$ ).

The calculated interatomic distances between the considered defects and neighboring atoms are listed in Table I. The values refer to the  $2 \times 2 \times 2$  supercell; test calculations with the PBEsol functional for the larger  $3 \times 3 \times 3$  supercell yield only minor differences, confirming that the lattice relaxation is confined to the immediate vicinity of the defects. Relative to the  $\text{Li}_{\text{Li}}\text{-O}_{\downarrow}$  and  $\text{Li}_{\text{Li}}\text{-O}_{\uparrow}$  distances in SLN, we find that the oxygen atoms move towards the antisite  $\text{Nb}_{\text{Li}}$  or interstitial  $\text{Nb}_{\text{V}}$  atoms in the case of systems with defects. The resulting

distances, and hence the volume contraction of the oxygen octahedra, are in fact almost identical for  $\text{Nb}_{\text{Li}}$  and  $\text{Nb}_{\text{V}}\text{-V}_{\text{Li}}$  as well as for  $\text{Nb}_{\text{Li}}$  in ilmenite LN. This observation is noteworthy because it is often claimed that compressive strain prevents the formation of interstitial niobium defects [44]. Furthermore, the  $\text{Li}_{\text{Li}}\text{-O}_{\downarrow}$  distance in stoichiometric ilmenite LN is markedly larger than for the ordinary stacking sequence, giving rise to the largest oxygen octahedra among the considered structures.

TABLE I. Interatomic distances calculated with the PBEsol and HSE06 functionals in the  $2 \times 2 \times 2$  supercell (in Å) compared with literature values.  $X$  stands for  $\text{Li}_{\text{Li}}$  in the case of SLN and ILN and for antisite  $\text{Nb}_{\text{Li}}$  or interstitial  $\text{Nb}_{\text{V}}$  in the case of defects; in Fig. 1, the atoms referenced as  $X$  are marked by an arrow for each structure. The symbols  $\text{O}_{\downarrow}$ ,  $\text{O}_{\uparrow}$ , and  $\text{Nb}_{\text{near}}$  indicate oxygen atoms below and above  $X$  according to the orientation in Fig. 1 and the nearest Nb atom, respectively. The electronic configuration is  $\text{Nb}^{5+}$  ( $4d^0$ ).

PBEsol	$X\text{-O}_{\downarrow}$	$X\text{-O}_{\uparrow}$	$X\text{-Nb}_{\text{near}}$
$\text{Li}_{\text{Li}}$ (SLN)	2.050 2.068 <sup>a</sup>	2.238 2.238 <sup>a</sup>	3.009 3.010 <sup>a</sup>
$\text{Nb}_{\text{Li}}$ (SLN)	1.916	2.086	3.084 3.032 <sup>b</sup>
$\text{Nb}_{\text{V}}$	1.980	1.970	2.801
$\text{Nb}_{\text{V}}\text{-V}_{\text{Li}}$	2.092	1.918	2.927
$\text{Li}_{\text{Li}}$ (ILN)	2.141	2.240	3.014
$\text{Nb}_{\text{Li}}$ (ILN)	1.935	2.069	3.058
HSE06	$X\text{-O}_{\downarrow}$	$X\text{-O}_{\uparrow}$	$X\text{-Nb}_{\text{near}}$
$\text{Li}_{\text{Li}}$ (SLN)	2.051	2.251	3.031
$\text{Nb}_{\text{Li}}$ (SLN)	1.906	2.088	3.105
$\text{Nb}_{\text{V}}$	1.974	1.966	2.811
$\text{Nb}_{\text{V}}\text{-V}_{\text{Li}}$	2.088	1.911	2.927
$\text{Li}_{\text{Li}}$ (ILN)	2.138	2.268	3.042
$\text{Nb}_{\text{Li}}$ (ILN)	1.919	2.080	3.074

<sup>a</sup>Reference [43]; experimental x-ray diffraction at 24 °C.

<sup>b</sup>Reference [17]; DFT+ $U$  calculation with  $U_{\text{eff}} = 4$  eV.

The nearest niobium atom referred to in the last column of Table I is above the defect for all configurations except for those involving  $\text{Nb}_V$ , where it is below, because the interstitial niobium atom is positioned in a different layer of the stacked crystal structure (see Fig. 1). Consequently, the roles of the  $\text{O}_\downarrow$  and  $\text{O}_\uparrow$  atoms below and above the defect are also reversed in this case. We find larger changes in the  $\text{Nb-Nb}_{\text{near}}$  distances for interstitials than for antisites, which is natural, as the former are more strongly confined to the crystal  $c$  axis.

The interatomic distances obtained with the HSE06 hybrid functional are very close to the corresponding PBEsol values, but it should be noted again that identical lattice constants were used in both cases. Furthermore, our results are in good agreement with the experimental data for SLN [43] and with the DFT+ $U$  calculations of Nahm and Park [17] for the  $\text{Nb}_{\text{Li}}$  antisite in SLN.

### C. Polarons

A polaron consists of an excess electron trapped at a single lattice site through lattice deformations. The prototypical small bound polaron in LN is centered at an isolated  $\text{Nb}_{\text{Li}}$  antisite, but polarons may also form when electrons become trapped at interstitial  $\text{Nb}_V$  sites, either isolated or paired with  $\text{V}_{\text{Li}}$  vacancies. In the following, we study the electron capture associated with the  $\text{Nb}^{5+} (4d^0) \rightarrow \text{Nb}^{4+} (4d^1)$  transition for all defect types using the PBEsol and HSE06 functionals, and we discuss their structural, electronic, and optical properties. To model the formation of polarons, we introduce one extra electron per supercell, which subsequently becomes trapped at the defect site; the increase in the electronic charge entails an appropriate reduction in the homogeneous negative background charge, so that the overall supercell is again charge neutral.

In Table II we report the relaxed interatomic distances around the defects obtained with the electronic configuration  $4d^1$  instead of  $4d^0$  as in Table I. As a consequence of the electron capture, the  $\text{Nb-Nb}_{\text{near}}$  distances decrease between 0.11 Å for  $\text{Nb}_{\text{Li}}$  (SLN) and 0.21 Å for  $\text{Nb}_V\text{-V}_{\text{Li}}$ . The largest  $\text{Nb-Nb}_{\text{near}}$  distance is found for  $\text{Nb}_{\text{Li}}$  in ILN, and the shortest

TABLE II. Interatomic distances (in Å) for intrinsic defects in SLN and ILN with the electronic configuration  $\text{Nb}^{4+} (4d^1)$ . For the notation see the caption of Table I. Changes in bond lengths here reflect the different charge states of the defects.

PBEsol	$X\text{-O}_\downarrow$	$X\text{-O}_\uparrow$	$X\text{-Nb}_{\text{near}}$
$\text{Nb}_{\text{Li}}$ (SLN)	2.000	2.097	2.977 2.890 <sup>a</sup>
$\text{Nb}_V$	2.004	2.028	2.629
$\text{Nb}_V\text{-V}_{\text{Li}}$	2.088	1.981	2.720
$\text{Nb}_{\text{Li}}$ (ILN)	2.036	2.093	3.053
HSE06	$X\text{-O}_\downarrow$	$X\text{-O}_\uparrow$	$X\text{-Nb}_{\text{near}}$
$\text{Nb}_{\text{Li}}$ (SLN)	1.997	2.096	3.001
$\text{Nb}_V$	1.989	2.026	2.611
$\text{Nb}_V\text{-V}_{\text{Li}}$	2.080	1.968	2.694
$\text{Nb}_{\text{Li}}$ (ILN)	2.028	2.092	3.060

<sup>a</sup>Reference [17]; DFT+ $U$  calculation with  $U_{\text{eff}} = 4$  eV.

is found for  $\text{Nb}_V$ . The deviation from the value given by Nahm and Park [17] for the  $\text{Nb}_{\text{Li}}$  (SLN) antisite can be ascribed to the fact that their calculations did not include effects of spin polarization. The Nb-O distances are again similar for  $\text{Nb}_{\text{Li}}$  (SLN),  $\text{Nb}_V\text{-V}_{\text{Li}}$ , and  $\text{Nb}_{\text{Li}}$  (ILN). This pronounced lattice relaxation is characteristic for the formation of polarons. Furthermore, as illustrated in Fig. 3, the charge density associated with the occupied  $4d^1$  state inside the electronic band gap is indeed strongly localized at the defect site, corroborating the formation of a small polaron.

Usually, the occupation of a localized defect level raises its energy due to the Coulomb repulsion. The opposite is true for polarons, however: The energy levels are lowered in this case because the gain due to the large lattice relaxation of the neighboring atoms outweighs the increase due to the Coulomb repulsion. The resulting energetic separation between the defect level and the conduction-band minimum derived with the HSE06 hybrid functional amounts to 1.37, 2.08, 1.66, and 1.61 eV for  $\text{Nb}_{\text{Li}}$  (SLN),  $\text{Nb}_V$ ,  $\text{Nb}_V\text{-V}_{\text{Li}}$ , and  $\text{Nb}_{\text{Li}}$  (ILN), respectively. Without the trapped electron and the polaronic lattice deformation, the defect level is resonant with the conduction bands. Of course, these band-structure transition energies cannot be immediately interpreted as optical absorption lines because they ignore the attractive electron-hole interaction and the selection rules for actual optical transitions. Nevertheless, we believe that  $\text{Nb}_V$  can be excluded as a possible explanation for the experimentally observed absorption peak at 1.64 eV on the basis of these results because the calculated energy deviates by more than 0.4 eV from the measured position. In addition, we do not consider  $\text{Nb}_{\text{Li}}$  in ilmenite LN further because, as we show below, the calculated energy levels of the polaron and the bipolaron coincide in this case, in contradiction to the experimental findings, which confirm a clear splitting. We thus carry out TDDFT calculations that account for many-body effects beyond the IPA only for  $\text{Nb}_{\text{Li}}$  (SLN) and  $\text{Nb}_V\text{-V}_{\text{Li}}$ . For this purpose, we apply a scissors shift to our PBEsol results that opens the energy gap between the occupied defect level and the unoccupied conduction bands (yellow arrow in Fig. 3) to the value obtained with the HSE06 hybrid functional (red arrow in Fig. 3). Scissors shifts of 0.60 and 0.85 eV are obtained for  $\text{Nb}_{\text{Li}}$  (SLN) and  $\text{Nb}_V\text{-V}_{\text{Li}}$  in this way, respectively. The difference of 0.25 eV reflects the fact that the DFT+ $U$  method based on PBEsol and the HSE06 functionals have different effects for the two defect types: In the first case, the parameter  $U$  has a constant value and equally localizes the electron density of defect states in different systems, whereas the more complicated exact exchange potential incorporated in the hybrid functional yields more system-specific energy contributions.

Our TDDFT results are displayed in Fig. 4 for the two different defect concentrations considered here, which correspond to the  $2 \times 2 \times 2$  (H) and the  $3 \times 3 \times 3$  (L) supercells. As all defects give rise to polarons in our simulations, the polaron concentration is identical to the defect concentration and hence more than 3 times higher in calculations for the  $2 \times 2 \times 2$  supercell than for the  $3 \times 3 \times 3$  supercell. Consequently, the oscillator strengths differ by the same factor. For all configurations, we find that the absorption peak lies between 1.5 and 2.0 eV, but as the energetic separation between the

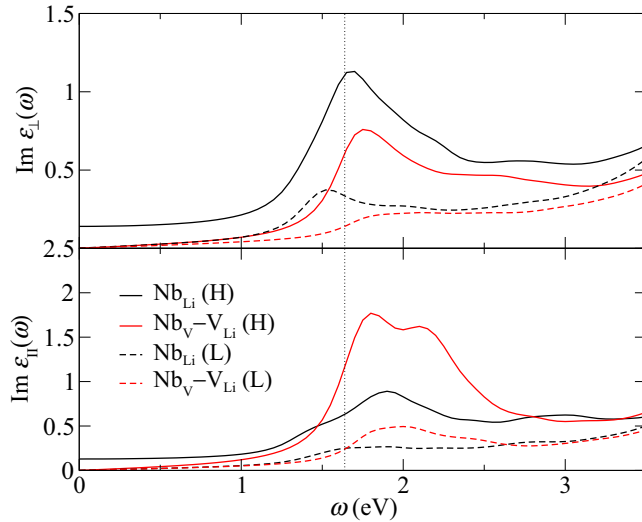


FIG. 4. Imaginary part of the dielectric function from TDDFT. Polaron absorption occurs around 1.7 eV. H denotes a high defect concentration with Li:Nb = 88%, and L denotes a low defect concentration with Li:Nb = 96%. The different cell sizes and defect concentrations explain the different oscillator strengths of the curves. The dotted vertical line marks the experimentally observed peak maximum at 1.64 eV.

defect level and the conduction bands is smaller for  $\text{Nb}_{\text{Li}}$  (SLN) than for  $\text{Nb}_{\text{V}}-\text{V}_{\text{Li}}$ , absorption occurs at a slightly lower energy in the case of  $\text{Nb}_{\text{Li}}$  (SLN). While the absorption peaks corresponding to the two defect types are close to each other for the lower defect concentration, marked differences can be made out for the higher concentration. This is related to the fact that the lattice structure is more strongly distorted by the niobium interstitial than by the antisite, indicated by the much smaller distance to the nearest Nb atom in the last column of Table II. In simulations using the smaller supercell, this leads to a strong interaction between the interstitials, whereas this effect is negligible in the case of the bigger supercell. For the antisite, the size of the supercell plays a less important role.

Furthermore, we note differences in the spectral line shape between the extraordinary and ordinary dielectric functions: For  $\varepsilon_{\parallel}(\omega)$ , the polaron absorption is generally broader, and the peaks are less clearly identifiable than for  $\varepsilon_{\perp}(\omega)$ .

Regarding the available measurements, which suggest a polaron peak at 1.64 eV, both models,  $\text{Nb}_{\text{Li}}$  (SLN) and  $\text{Nb}_{\text{V}}-\text{V}_{\text{Li}}$ , are compatible with the experimental results. The absorption peak corresponding to  $\text{Nb}_{\text{Li}}$  (SLN) with the lower defect concentration lies slightly below the measured value, whereas the other models yield energetic positions that are blueshifted by a similar amount.

#### D. Bipolarons

The localization of a second electron at a polaron center results in the formation of a bipolaron. Prototypical bipolarons in LN occur at  $\text{Nb}_{\text{Li}}-\text{Nb}_{\text{Nb}}$  pairs, extending over two lattice sites, as illustrated in Fig. 5. The electronic configuration is denoted  $\text{Nb}_{\text{Li}}^{4+}-\text{Nb}_{\text{Nb}}^{4+}$  ( $4d^1-4d^1$ ). However, other defect types might also give rise to bipolarons. Here we take all defects into consideration that we also studied previously in the context of small polarons.

The calculated interatomic distances in Table III show that the  $\text{Nb}-\text{Nb}_{\text{near}}$  distances are further contracted due to the additional negative charge. The interstitials again exhibit notably shorter distances to the nearest Nb atom than the antisites. As Nahm and Park [17] pointed out before, the defect levels are decreased in energy as the two niobium atoms move closer together. As shown in Fig. 5, the bipolaron levels for  $\text{Nb}_{\text{V}}$  and  $\text{Nb}_{\text{V}}-\text{V}_{\text{Li}}$  are at least 0.4 eV lower than for  $\text{Nb}_{\text{Li}}$  (SLN) when calculated with the HSE06 hybrid functional. In detail, the separation from the conduction-band minimum equals 1.57, 2.26, 2.08, and 1.63 eV for  $\text{Nb}_{\text{Li}}$  (SLN),  $\text{Nb}_{\text{V}}$ ,  $\text{Nb}_{\text{V}}-\text{V}_{\text{Li}}$ , and  $\text{Nb}_{\text{Li}}$  (ILN), respectively. As already noted above, the bipolaron level for  $\text{Nb}_{\text{Li}}$  (ILN) is thus at the same position as the polaron level, in contradiction to the experimental findings. Therefore, we rule this defect type out as a model to explain the experimental data. For the  $\text{Nb}_{\text{Li}}$  (SLN) antisite, we find that the lattice relaxation induced by the formation of a bipolaron

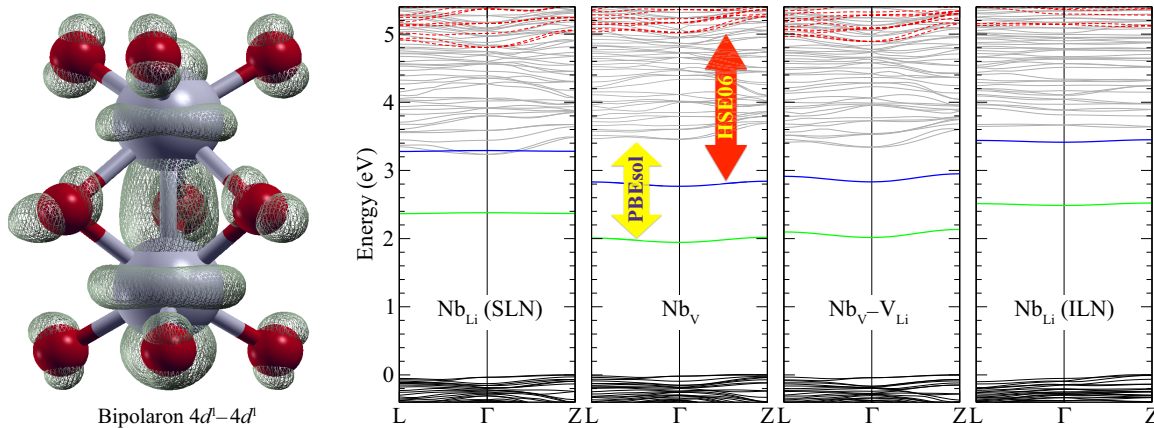


FIG. 5. Left: The electronic charge density associated with the bipolaron at the  $\text{Nb}_{\text{Li}}$  (SLN) antisite is not localized at one lattice site but extends to the nearest  $\text{Nb}_{\text{Nb}}$  atom, forming a hybridized  $4d^1-4d^1$  orbital. This is true for all defect types. Right: Electronic band structures for all considered defects. The color scheme is the same as in Fig. 3. The energy separation from the bipolaron levels to the conduction bands is indicated by yellow (PBEsol) and red (HSE06) arrows. The two structures containing interstitial  $\text{Nb}_{\text{V}}$  atoms exhibit the largest separation from the conduction bands and are therefore the best models to explain the experimentally observed absorption peak at 2.5 eV.

TABLE III. Interatomic distances (in Å) for intrinsic defects in SLN and ILN with the electronic configuration  $\text{Nb}_{\text{Li}}^{4+}\text{-Nb}_{\text{Nb}}^{4+}$  ( $4d^1\text{-}4d^1$ ). For the notation see the caption of Table I. The bipolaron extends over two lattice sites, thereby inducing a strong contraction of the distance to the nearest Nb atom.

PBEsol	$X\text{-O}_\downarrow$	$X\text{-O}_\uparrow$	$X\text{-Nb}_{\text{near}}$
$\text{Nb}_{\text{Li}}$ (SLN)	2.051	2.070	2.639 2.639 <sup>a</sup>
$\text{Nb}_V$	2.016	2.066	2.469
$\text{Nb}_V\text{-V}_{\text{Li}}$	2.066	2.037	2.519
$\text{Nb}_{\text{Li}}$ (ILN)	2.085	2.067	2.691
HSE06	$X\text{-O}_\downarrow$	$X\text{-O}_\uparrow$	$X\text{-Nb}_{\text{near}}$
$\text{Nb}_{\text{Li}}$ (SLN)	2.047	2.068	2.626
$\text{Nb}_V$	2.004	2.074	2.452
$\text{Nb}_V\text{-V}_{\text{Li}}$	2.056	2.045	2.494
$\text{Nb}_{\text{Li}}$ (ILN)	2.095	2.054	2.656

<sup>a</sup>Reference [17]; DFT+ $U$  calculation with  $U_{\text{eff}} = 4$  eV.

effectively only lowers the  $4d^1$  state at the  $\text{Nb}_{\text{Nb}}$  site, whereas the strong relaxation of the  $\text{Nb}_V\text{-V}_{\text{Li}}$  defect pair leads to an increased deep trapping of both electrons at  $\text{Nb}_{\text{Nb}}$  and  $\text{Nb}_{\text{Li}}$ .

Our TDDFT results are shown in Fig. 6. Scissors shifts of 0.66 and 0.73 eV are applied for  $\text{Nb}_{\text{Li}}$  and  $\text{Nb}_V\text{-V}_{\text{Li}}$ , respectively, in accordance with the procedure outlined above. The HSE06 hybrid functional increases the difference between the energetic positions of the defect levels only marginally in this case because the scissors shifts are almost identical. In contrast to Fig. 4, there are now clear differences in the calculated spectra between  $\text{Nb}_{\text{Li}}$  (SLN) and  $\text{Nb}_V\text{-V}_{\text{Li}}$ . Generally, the absorption peaks for  $\text{Nb}_V\text{-V}_{\text{Li}}$  are blueshifted by at least 0.5 eV with respect to  $\text{Nb}_{\text{Li}}$  (SLN), except for the ordinary

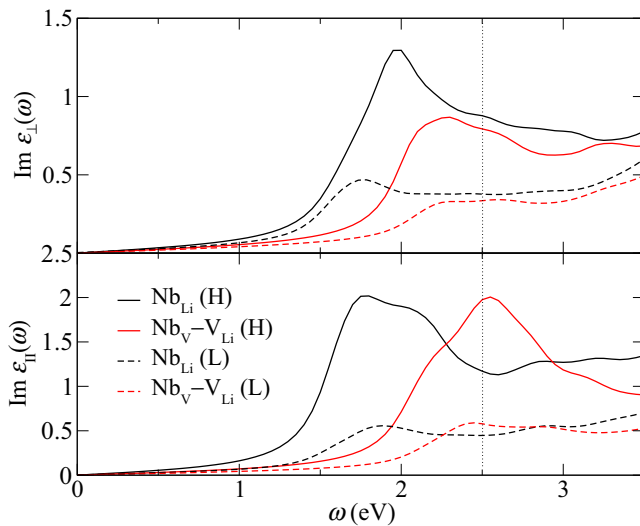


FIG. 6. Imaginary part of the dielectric function from TDDFT. The bipolaron absorption peaks for  $\text{Nb}_{\text{Li}}$  and  $\text{Nb}_V\text{-V}_{\text{Li}}$  are clearly positioned at distinct energies. H denotes a high defect concentration with  $\text{Li:Nb} = 88\%$ , and L denotes a low defect concentration with  $\text{Li:Nb} = 96\%$ . The different cell sizes and defect concentrations explain the different oscillator strengths of the curves. The dotted vertical line marks the experimentally observed peak maximum at 2.5 eV.

TABLE IV. Total energy of a single  $\text{Nb}_{\text{Li}}$  (SLN) antisite (in eV) relative to the  $\text{Nb}_V\text{-V}_{\text{Li}}$  defect pair calculated with PBEsol (DFT+ $U$ ) and HSE06 for the different charge states. Larger supercells or different exchange-correlation functionals do not qualitatively alter the results.

Configuration	$4d^0$	$4d^1$	$4d^1\text{-}4d^1$
PBEsol ( $2 \times 2 \times 2$ )	-0.619	-0.695	-0.164
PBEsol ( $3 \times 3 \times 3$ )	-0.669	-0.683	-0.140
HSE06 ( $2 \times 2 \times 2$ )	-0.694	-0.676	-0.132

dielectric function  $\varepsilon_\perp(\omega)$  in the case of the higher defect concentration, where  $\text{Nb}_V\text{-V}_{\text{Li}}$  exhibits a broad absorption range around 2.4 eV. The maximum of the absorption peak for the bipolaron at the antisite defect in SLN is only slightly blueshifted with respect to the polaron at the same defect, displayed in Fig. 4. This small separation does not match the distance between the experimentally observed absorption peak and the one centered at 2.5 eV, which is usually ascribed to the  $\text{Nb}_{\text{Li}}^{4+}\text{-Nb}_{\text{Nb}}^{4+}$  ( $4d^1\text{-}4d^1$ ) bipolaron. In contrast, the positions of the absorption maxima for  $\text{Nb}_V\text{-V}_{\text{Li}}$  obtained here are in good agreement with the experimental findings.

The total energies of the  $\text{Nb}_{\text{Li}}$  antisite in SLN and the  $\text{Nb}_V\text{-V}_{\text{Li}}$  defect complex can be directly compared because they contain the same number of atoms. Our calculated total-energy differences for the various charge states are listed in Table IV. Overall, the antisite defect is energetically favored by about 0.7 eV for the lower charge states  $4d^0$  and  $4d^1$ . For the  $4d^1\text{-}4d^1$  configuration, this energy difference is reduced to about 0.15 eV, however. For comparison, the antisite defect in ilmenite LN is less stable by at least 1.8 eV ( $4d^1\text{-}4d^1$ ).

Xu *et al.* [11] and Li *et al.* [13] calculated the absolute formation energy of the  $\text{Nb}_{\text{Li}}$  antisite, together with those of other defects in SLN, and concluded that it occurs spontaneously. Interpreting our results in relation to the formation energy for the antisite defect obtained by Li *et al.*, it is likely that the  $\text{Nb}_V\text{-V}_{\text{Li}}$  defect pair appears spontaneously, too. According to Table IV, the difference in the formation energies of bipolarons at these defect types is much smaller than that of polarons. As a consequence, if the Fermi level is raised, the transition from the  $4d^1$  to the  $4d^1\text{-}4d^1$  charge state takes place earlier for the interstitial than for the antisite defect. This is a clear indication that bipolarons form preferentially at  $\text{Nb}_V\text{-V}_{\text{Li}}$  complexes rather than at antisite defects.

Finally, to assess the relative stability of the  $\text{Nb}_V\text{-V}_{\text{Li}}$  defect pair with respect to  $\text{Nb}_{\text{Li}}$ , we employ the nudged-elastic-band method [45] to compute the diffusion barrier. We choose ten images along a pathway where the atomic configurations of  $\text{Nb}_{\text{Li}}$  and  $\text{Nb}_V\text{-V}_{\text{Li}}$  constitute the start and end positions, connected with spring constants between 310 and 470  $\text{kg/s}^2$ . Although the antisite is energetically favored, the  $\text{Nb}_V$  defect does not swap sites to become an antisite because of the high energy barriers of 0.86, 0.84, and 1.61 eV for the  $4d^0$ ,  $4d^1$ , and  $4d^1\text{-}4d^1$  charge states, respectively.

#### IV. CONCLUSIONS

We have calculated the ionic and electronic structures of different point defects and simple defect complexes in lithium

niobate and modeled the electronic polarons and bipolarons therein. In all investigated defect models, i.e.,  $\text{Nb}_{\text{Li}}$  (SLN),  $\text{Nb}_{\text{V}}$ ,  $\text{Nb}_{\text{V}}\text{-V}_{\text{Li}}$ , and  $\text{Nb}_{\text{Li}}$  (ILN), we observe the formation of polarons at the defect site as well as bipolarons that extend over two lattice sites at  $\text{Nb}_{\text{Li}}\text{-Nb}_{\text{Nb}}$  and  $\text{Nb}_{\text{V}}\text{-Nb}_{\text{Nb}}$  pairs. We analyzed the positions of the defect levels inside the band gap and the (bi)polaron absorption patterns in the dielectric functions. As for the polaron absorption, we conclude that three defect models, namely,  $\text{Nb}_{\text{Li}}$  (SLN),  $\text{Nb}_{\text{V}}\text{-V}_{\text{Li}}$ , and  $\text{Nb}_{\text{Li}}$  (ILN), yield absorption peaks whose positions are in agreement with the experimental findings. In the case of bipolarons, only the models with an interstitial niobium atom,  $\text{Nb}_{\text{V}}$  and  $\text{Nb}_{\text{V}}\text{-V}_{\text{Li}}$ , exhibit defect levels that are sufficiently below the conduction-band minimum to give rise to an absorption peak near 2.5 eV, as experimentally

observed. Our TDDFT results confirm that polarons and bipolarons for  $\text{Nb}_{\text{V}}\text{-V}_{\text{Li}}$  show distinct absorption peaks in the dielectric functions. Overall, we find that this model has the best agreement with the experimental data. In contrast, the  $\text{Nb}_{\text{Li}}$  (SLN) antisite model cannot satisfactorily explain the experimental findings, as there is no clear separation of 0.9 eV between the polaron and the bipolaron absorption peak in this case.

## ACKNOWLEDGMENTS

All calculations were performed at the Paderborn Center for Parallel Computing (PC<sup>2</sup>). We gratefully acknowledge financial support by the Deutsche Forschungsgemeinschaft (DFG) via Sonderforschungsbereich TRR 142, Project B04.

- 
- [1] T. Volk and M. Wöhlecke, *Lithium Niobate, Defects, Photo-refraction and Ferroelectric Switching*, Springer Series in Materials Science Vol. 115 (Springer, Berlin, 2009).
- [2] P. Lerner, C. Legras, and J. P. Dumas, *J. Cryst. Growth* **3**, 231 (1968).
- [3] G. E. Peterson and A. Carnevale, *J. Chem. Phys.* **56**, 4848 (1972).
- [4] N. Iyi, K. Kitamura, F. Izumi, J. K. Yamamoto, T. Hayashi, H. Asano, and S. Kimura, *J. Solid State Chem.* **101**, 340 (1992).
- [5] A. P. Wilkinson, A. K. Cheetham, and R. H. Jarman, *J. Appl. Phys.* **74**, 3080 (1993).
- [6] N. Zotov, H. Boysen, F. Frey, T. Metzger, and E. Born, *J. Phys. Chem. Solids* **55**, 145 (1994).
- [7] S. C. Abrahams and P. Marsh, *Acta Crystallogr., Sect. B* **42**, 61 (1986).
- [8] H. Donnerberg, S. M. Tomlinson, C. R. A. Catlow, and O. F. Schirmer, *Phys. Rev. B* **40**, 11909 (1989).
- [9] D. M. Smyth, *Ferroelectrics* **50**, 93 (1983).
- [10] A. Mehta, A. Navrotsky, N. Kumada, and N. Kinomura, *J. Solid State Chem.* **102**, 213 (1993).
- [11] H. Xu, D. Lee, J. He, S. B. Sinnott, V. Gopalan, V. Dierolf, and S. R. Phillpot, *Phys. Rev. B* **78**, 174103 (2008).
- [12] Y. Li, W. G. Schmidt, and S. Sanna, *Phys. Rev. B* **91**, 174106 (2015).
- [13] Y. Li, W. G. Schmidt, and S. Sanna, *Phys. Rev. B* **89**, 094111 (2014); Y. Li, S. Sanna, and W. G. Schmidt, *J. Phys. Chem.* **140**, 234113 (2014).
- [14] O. F. Schirmer, M. Imlau, C. Merschjann, and B. Schoke, *J. Phys. Condens. Matter* **21**, 123201 (2009).
- [15] K. L. Sweeney and L. E. Halliburton, *Appl. Phys. Lett.* **43**, 336 (1983).
- [16] J. Koppitz, O. F. Schirmer, and A. I. Kuznetsov, *Europhys. Lett.* **4**, 1055 (1987).
- [17] H. H. Nahm and C. H. Park, *Phys. Rev. B* **78**, 184108 (2008).
- [18] A. Riefer, S. Sanna, A. Schindlmayr, and W. G. Schmidt, *Phys. Rev. B* **87**, 195208 (2013).
- [19] P. Rinke, A. Schleife, E. Kioupakis, A. Janotti, C. Rödl, F. Bechstedt, M. Scheffler, and C. G. Van de Walle, *Phys. Rev. Lett.* **108**, 126404 (2012).
- [20] S. Botti, A. Schindlmayr, R. Del Sole, and L. Reining, *Rep. Prog. Phys.* **70**, 357 (2007).
- [21] L. Reining, V. Olevano, A. Rubio, and G. Onida, *Phys. Rev. Lett.* **88**, 066404 (2002).
- [22] S. Botti, F. Sottile, N. Vast, V. Olevano, L. Reining, H.-C. Weissker, A. Rubio, G. Onida, R. Del Sole, and R. W. Godby, *Phys. Rev. B* **69**, 155112 (2004).
- [23] P. Giannozzi, S. Baroni, N. Bonini, M. Calandra, R. Car, C. Cavazzoni, D. Ceresoli, G. L. Chiarotti, M. Cococcioni, I. Dabo, A. Dal Corso, S. de Gironcoli, S. Fabris, G. Fratesi, R. Gebauer, U. Gerstmann, C. Gougoussis, A. Kokalj, M. Lazzeri, L. Martin-Samos, N. Marzari, F. Mauri, R. Mazzarello, S. Paolini, A. Pasquarello, L. Paulatto, C. Sbraccia, S. Scandolo, G. Sclauzero, A. P. Seitsonen, A. Smogunov, P. Umari, and R. M. Wentzcovitch, *J. Phys. Condens. Matter* **21**, 395502 (2009).
- [24] D. R. Hamann, *Phys. Rev. B* **88**, 085117 (2013).
- [25] J. P. Perdew, A. Ruzsinszky, G. I. Csonka, O. A. Vydrov, G. E. Scuseria, L. A. Constantin, X. Zhou, and K. Burke, *Phys. Rev. Lett.* **100**, 136406 (2008).
- [26] M. Friedrich, A. Riefer, S. Sanna, W. G. Schmidt, and A. Schindlmayr, *J. Phys. Condens. Matter* **27**, 385402 (2015).
- [27] M. Friedrich, A. Schindlmayr, W. G. Schmidt, and S. Sanna, *Phys. Status Solidi B* **253**, 683 (2016).
- [28] F. Schmidt, M. Landmann, E. Rauls, N. Argiolas, S. Sanna, W. G. Schmidt, and A. Schindlmayr, *Adv. Mater. Sci. Eng.* **2017**, 3981317 (2017).
- [29] A. Sanson, A. Zaltron, N. Argiolas, C. Sada, M. Bazzan, W. G. Schmidt, and S. Sanna, *Phys. Rev. B* **91**, 094109 (2015).
- [30] M. Cococcioni and S. de Gironcoli, *Phys. Rev. B* **71**, 035105 (2005).
- [31] J. Heyd, G. E. Scuseria, and M. Ernzerhof, *J. Chem. Phys.* **118**, 8207 (2003); A. V. Krukau, O. A. Vydrova, A. F. Izmaylov, and G. E. Scuseria, *ibid.* **125**, 224106 (2006).
- [32] A. Marini, C. Hogan, M. Grüning, and D. Varsano, *Comput. Phys. Commun.* **180**, 1392 (2009).
- [33] M. Friedrich, W. G. Schmidt, A. Schindlmayr, and S. Sanna, *Phys. Rev. Mater.* **1**, 034401 (2017).
- [34] S. Sharma, J. K. Dewhurst, A. Sanna, and E. K. U. Gross, *Phys. Rev. Lett.* **107**, 186401 (2011).
- [35] S. Rigamonti, S. Botti, V. Veniard, C. Draxl, L. Reining, and F. Sottile, *Phys. Rev. Lett.* **114**, 146402 (2015).

- [36] H. Boysen and F. Altorfer, *Acta Crystallogr., Sect. B* **50**, 405 (1994).
- [37] A. Riefer, M. Friedrich, S. Sanna, U. Gerstmann, A. Schindlmayr, and W. G. Schmidt, *Phys. Rev. B* **93**, 075205 (2016).
- [38] D. Redfield and W. J. Burke, *J. Appl. Phys.* **45**, 4566 (1974).
- [39] S. Kase and K. Ohi, *Ferroelectrics* **8**, 419 (1974).
- [40] A. Dhar and A. Mansingh, *J. Appl. Phys.* **68**, 5804 (1990).
- [41] Z. Jiangou, Z. Shipin, X. Dingquan, W. Xiu, and X. Guanfeng, *J. Phys. Condens. Matter* **4**, 2977 (1992).
- [42] C. Thierfelder, S. Sanna, A. Schindlmayr, and W. G. Schmidt, *Phys. Status Solidi C* **7**, 362 (2010).
- [43] S. C. Abrahams, J. M. Reddy, and J. L. Bernstein, *J. Phys. Chem. Solids* **27**, 997 (1966).
- [44] K. Nassau and M. E. Lines, *J. Appl. Phys.* **41**, 533 (1970).
- [45] H. Jónsson, G. Mills, and K. W. Jacobsen, in *Classical and Quantum Dynamics in Condensed Phase Simulations*, edited by B. J. Berne, G. Ciccotti, and D. F. Coker (World Scientific, Singapore, 1998), p. 385.